



<https://creativecommons.org/licenses/by-nc-nd/4.0>

Spatio-temporal evolution of rift volcanism controlled top-down by a deepening graben

Gaetano Ferrante^{a,b}, Eleonora Rivalta^{a,c}, Francesco Maccaferri^d

^aDipartimento di Fisica e Astronomia, Alma Mater Studiorum - Università di Bologna, Viale Bertini Pichat, 8, Bologna, 40126, Italy

^bDepartment of Earth, Environmental and Planetary Sciences, Rice University, 6100 Main Street, Houston, 77005, Texas, USA

^cHelmholtz Centre Potsdam GFZ German Research Centre for Geosciences, Telegrafenberg, Potsdam, 14473, Germany

^dIstituto Nazionale di Geofisica e Vulcanologia, Osservatorio Vesuviano, Napoli, 80124, Italy.

This manuscript version has been accepted for publication on EPSL on January 23rd, 2024. The article was originally submitted to EPSL on September 23rd, 2023; and Submitted in revised form on December 13th, 2023.

The final published version of this article is available online since January 31st, 2024:
<https://doi.org/10.1016/j.epsl.2024.118593>

1
2
3
4
5
6
7
8
9
10
11
12
13
14
15
16
17
18
19
20
21
22
23
24
25
26
27
28
29
30
31
32
33
34
35
36
37
38
39
40
41
42
43
44
45
46
47
48
49
50
51
52
53
54
55
56
57
58
59
60
61
62
63
64
65

Spatio-temporal evolution of rift volcanism controlled top-down by a deepening graben

Gaetano Ferrante^{a,b}, Eleonora Rivalta^{a,c}, Francesco Maccaferri^d

^a*Dipartimento di Fisica e Astronomia, Alma Mater Studiorum - Università di
Bologna, Viale Berti Pichat, 8, Bologna, 40126, Italy*

^b*Department of Earth, Environmental and Planetary Sciences, Rice University, 6100
Main Street, Houston, 77005, Texas, USA*

^c*Helmholtz Centre Potsdam GFZ German Research Centre for
Geosciences, Telegrafenberg, Potsdam, 14473, Germany*

^d*Istituto Nazionale di Geofisica e Vulcanologia (INGV), Osservatorio
Vesuviano, Napoli, 80124, Italy*

Abstract

Volcanism in continental rifts is generally observed to shift over time from the inside of the basin to its flanks and viceversa, but the controls on these switches are still unclear. Here we use numerical simulations of dike propagation to test the hypothesis that the spatio-temporal evolution of rift volcanism is controlled by the crustal stresses produced during the development of the rift basin. We find that the progressive deepening of a rift rotates the direction of the principal stresses under the basin, deflecting ascending dikes. This causes an early shift of volcanism from the inside of the graben to its flanks. The intensification of this stress pattern, due to further deepening of the basin, promotes the formation of lower crustal sill-like intrusions that can stack under the rift, shallowing the depth at which dikes nucleate, eventually causing a late stage of in-rift axial volcanism. Given the agreement between our model results and observations, we conclude that the temporal shifts in the location of rift volcanism are controlled to first order by the elastic

Preprint submitted to EPSL

December 13, 2023

1
2
3
4
5
6
7
8
9 stresses developing in the crust as the rift matures. We thereby suggest that
10 geodynamic models should account for elasticity and the redistribution of
11 surface loads in order to effectively reproduce rift-related magmatism.
12

13
14
15 *Keywords:* Rift magmatism, Dike propagation, Sill emplacement, Surface
16 loading, Elastic stresses
17
18

19 20 **1. Introduction**

21
22
23 Continental rifting is the process by which the continental lithosphere is
24 slowly thinned and deformed over timescales of millions of years, in response
25 to extensional forces of different origin that result in the formation of large
26 scale fault-bounded basins. Over such time scales, the weakest layers of the
27 lithosphere are expected to behave viscously. Consequently, numerical mod-
28 els of rifting usually assume visco-elasto-plastic rheologies for the lithosphere.
29 While geodynamic models effectively reproduce the deformation history of
30 rifts, they usually fail to capture the behavior of another fundamental feature
31 of rifted areas, that is the evolution of magmatism. Indeed, continental rifting
32 is often accompanied by volcanism (White, 1992), whose location is observed
33 to shift during a rift's lifetime. In particular, volcanism often migrates from
34 the inside of the rift graben (in-rift volcanism) to its flanks (off-rift volcan-
35 ism) during the early stages of rifting, and then back to the axial portion
36 during rift maturity. These patterns are commonly observed regardless of the
37 underlying cause of rifting or whether the rift is magma-rich or magma-poor,
38 suggesting a common control, despite the differences between individual rifts
39 and their specific complexities. However, in spite of the recent advances, the
40 mechanisms governing the spatio-temporal evolution of rift magmatism are
41

1
2
3
4
5
6
7
8
9
10
11
12
13
14
15
16
17
18
19
20
21
22
23
24
25
26
27
28
29
30
31
32
33
34
35
36
37
38
39
40
41
42
43
44
45
46
47
48
49
50
51
52
53
54
55
56
57
58
59
60
61
62
63
64
65
66

still poorly understood. The shifts in the loci of magmatic activity in rifts have often been explained in terms of their tectonic evolution, but the models advocated are usually ad-hoc and thus unable to capture the ubiquity of the observed patterns. A comprehensive model of rift magmatism needs to explain why rifts of very different nature and complexity share the following overarching observations: i) the temporal shifts in the location of eruptive vents (e.g. Michon and Merle, 2001; Liu et al., 2001; Corti, 2009), ii) the accumulation at depth of large magma volumes through the emplacement of multiple sill-like intrusions (Thybo and Nielsen, 2009; Thybo and Artemieva, 2013), iii) why the shifts from pattern to pattern occur relatively abruptly if compared to the overall duration of volcanism, marking well-defined ‘phases’, iv) and the fact that different phases of volcanism are often associated with differences in magma composition (Pasteels et al., 1989).

While no model so far has achieved an overarching explanation of the spatio-temporal and geochemical patterns described above, there have been attempts to explain some of the observed shifts, with many authors focusing on the counterintuitive locations of off-rift volcanoes. Some studies attributed the occurrence of flank volcanism to the interaction of magma with boundary faults (e.g. Bosworth, 1987; Corti et al., 2004). Bosworth (1987) ascribed the existence of off-rift volcanoes to the presence of low-angle detachment faults beneath asymmetric rifts, that would tap the asthenosphere and weaken the crust, facilitating magma migration far from the basin. Corti et al. (2004) used analogue models to propose that surface deformation controls the migration of magma towards the footwall of the boundary faults, that would in turn channel magma to the surface to feed off-rift volcanoes. However,

1
2
3
4
5
6
7
8
9
10 67 these interpretations are not fully supported by independent observations
11 68 for a number of reasons: in particular, there is little to no evidence of deeply
12
13 69 penetrating detachment faults underlying extensional areas (Ellis and King,
14
15 70 1991) and propagation of magma along faults is now considered to be a minor
16
17 71 mechanism (Pollard, 1987; Ziv et al., 2000). It is increasingly recognised
18
19 72 that, in all tectonic contexts, the overarching control on magma pathways
20
21 73 lies in the elastic stresses acting in the lithosphere (Anderson, 1937; Muller
22
23 74 and Pollard, 1977; Rubin, 1995; Rivalta et al., 2015). Regardless of the
24
25 75 mechanisms driving rifting and the production of melt in the mantle, once
26
27 76 magma reaches the lithosphere its ascent pathways will be controlled by
28
29 77 elastic stresses. In fact, magma transport through the lithosphere occurs
30
31 78 mostly through diking, a form of hydraulic fracturing (e.g. Rubin, 1995). As
32
33 79 predominantly opening fractures, dikes tend to open roughly in the direction
34
35 80 of least compression, rather than follow directions optimally oriented for
36
37 81 shearing, which would not accommodate efficiently the intruded magma (e.g.
38
39 82 Anderson, 1937; Weertman, 1971; Nakamura, 1977; Muller and Pollard, 1977;
40
41 83 Pollard, 1987; Dahm, 2000; Ziv et al., 2000; Watanabe et al., 2002).

42 84 Ellis and King (1991) suggested that flank volcanism in continental rifts
43
44 85 could be explained by the dilational strain caused at the base of the footwall
45
46 86 by faulting in a flexurally supported crust, which would favor upward magma
47
48 87 propagation provided that melt is available in the lower crust. Maccaferri
49
50 88 et al. (2014) proposed to include the unloading stresses induced by the for-
51
52 89 mation of the rift graben in the stress computations. They built a zero-order
53
54 90 stress model by superposing a negative strip load (simulating the surface
55
56 91 mass load missing in correspondence of the basin) to a uniform stretching of

1
2
3
4
5
6
7
8
9
10 92 the lithosphere. They then used a dike propagation code (Maccaferri et al.,
11 93 2010, 2011) based on the principles of linear fracture mechanics (Griffith,
12 94 1921; Dahm, 2000) to simulate magma ascent in such a ‘gravitationally un-
13 95 loaded’, extending rift. Their model predicts that when the stresses due to
14 96 the unloading of the graben dominate over the tectonic tension, the direction
15 97 of least compression becomes vertical in a depth range under the basin, turn-
16 98 ing ascending dikes into subhorizontal magma bodies or forcing their way up
17 99 to the rift flanks on oblique trajectories.

200 Here, we further test the Maccaferri et al. (2014) model against its ability
201 to predict the shifting through time of vent locations in rifts, along with the
202 overarching observations listed above, solely on the basis of the evolution of
203 unloading forces due to the deepening of the graben. To do so, we further
204 develop the modeling approach of Maccaferri et al. (2014) so that it accounts
205 for time-dependent stresses by including the following elements in the model:
206 a) time-dependent unloading due to a deepening graben subjected to sedi-
207 mentation, b) stress interaction between successive dike intrusions. We focus
208 most of our numerical simulations to the case of a full-graben. In addition,
209 our study extends to the case of a half-graben, in order to investigate whether
210 the asymmetric distribution of volcanism observed in many half-grabens (Ja-
211 necke et al., 1997; Bjorklund et al., 2002) can be explained in terms of the
212 stresses generated in the crust by an asymmetric graben.

213 With the purpose of developing a widely applicable idealized rifting model,
214 we keep the geometries simple and choose parameters of general relevance.
215 While inevitably resulting in decreased ability to match the complexity of
216 specific rift settings, this may promote a clearer understanding of the major

1
2
3
4
5
6
7
8
9
10
11
12
13
14
15
16
17
18
19
20
21
22
23
24
25
26
27
28
29
30
31
32
33
34
35
36
37
38
39
40
41
42
43
44
45
46
47
48
49
50
51
52
53
54
55
56
57
58
59
60
61
62
63
64
65

117 mechanisms controlling the spatio-temporal evolution of rift volcanism. This
118 would clarify the controls on several processes of global relevance, such as
119 underplating, the evolution of crustal rocks and the distribution of volcanism,
120 and may provide new important indications for state of the art geodynamic
121 models that aim to capture the evolution of magmatism and rift volcanism.

122 We first provide qualitative observations of the evolution of magmatism
123 in rifts to identify commonalities among different natural settings. Then,
124 we describe the stress model used in our simulations and the methods for
125 computing the resulting magma trajectories. Lastly, we describe the results
126 of our simulations, discuss implications and limitations of our model and
127 suggest possible future directions.

128 **2. Observations of Rift Magmatism**

129 *2.1. Main Ethiopian Rift*

130 Volcanism in the Main Ethiopian Rift (hereafter MER) started prior to
131 rift initiation, resulting in the eruption of voluminous flood basalts that
132 erupted in two separate episodes in the areas now comprising the Ethiopian
133 and Somalian plateaus (Fig. 1a; Bonini et al., 2005; Corti, 2009). Rifting
134 in the Northern MER and the formation of the Afar were accompanied and
135 followed by flood basalt volcanism inside the developing depression (Cher-
136 net et al., 1998). Subsequent volcanism was characterized by the occurrence
137 of ignimbrites and mafic lavas inside the graben and in the proximal part
138 of the flanks during the Mio-Pliocene (Chernet et al., 1998; Bonini et al.,
139 2005). Then, an important phase of off-rift volcanism took place during the
140 Pliocene, with the formation of basaltic central volcanoes on the flanks of

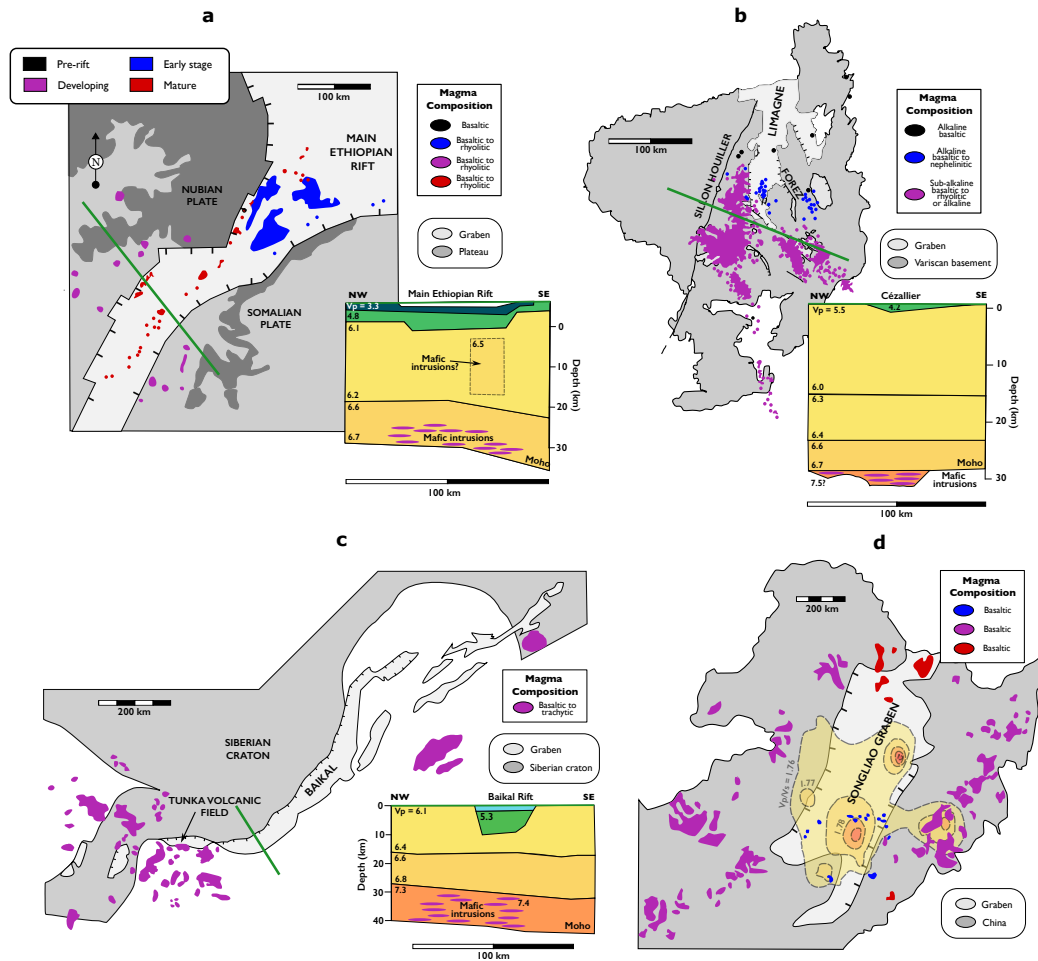


Figure 1: **a-d**: Examples of spatio-temporal evolution of rift magmatism. **a**: Main Ethiopian Rift. Data on the distribution of the volcanics are adapted from Chernet et al. (1998), Bonini et al. (2005) and Maccaferri et al. (2014). Inset shows V_p crustal profile to highlight the inferred presence of lower crustal mafic intrusions, modified from Mackenzie et al. (2005). **b**: Limagne Graben of the Massif Central Rift, France. Data on the distribution of the volcanics are adapted from Michon and Merle (2001). Inset shows the V_p crustal profile, modified from Zeyen et al. (1997). **c**: Baikal Rift, Russia. Data on the distribution of the volcanics are adapted from Ivanov and Demonerova (2010). Inset shows the V_p crustal profile, modified from Thybo and Nielsen (2009). **d**: Songliao Graben, China. Data on the distribution of the volcanics are adapted from Liu et al. (2001). Inset shows contours of V_p/V_s ratio beneath the graben, with higher values interpreted to represent crustal intrusions, modified from He et al. (2014). The colors associated with each magmatic phase reflect those used for the results of our simulations (Fig. 8).

1
2
3
4
5
6
7
8
9 141 the graben (Bonini et al., 2005). A subsequent rifting phase coincided with
10 142 the deactivation of the boundary faults and the focusing of volcanism in the
11 143 inner portion of the graben, as part of the transition to seafloor spreading, fo-
12 144 cusing the recent Quaternary volcanics within the Wonji Fault Belt (Ebinger
13 145 and Casey, 2001; Bonini et al., 2005; Corti, 2009). The East African Rift
14 146 System is also characterized by the presence of lower crustal sill-like mag-
15 147 matic intrusions: Birt et al. (1997) observed a strongly reflective lower crust
16 148 directly below the Kenya Rift Graben, coherent with the presence of a high
17 149 velocity underplated layer, while Mackenzie et al. (2005) explained variations
18 150 in seismic reflectivity in the lower crust beneath the Main Ethiopian Rift in
19 151 terms of layered sills. In addition to the lower crustal layered intrusions, Ker-
20 152 anen et al. (2004) and Mackenzie et al. (2005) also identified a high velocity
21 153 region beneath the rift axis. The latter has been interpreted as mafic intru-
22 154 sions feeding the magmatic centers of the rift valley through upper crustal
23 155 dikes, marking a zone of focused magmatism representing a protoridge axis
24 156 for future seafloor spreading (Keranen et al., 2004).

25 157 *2.2. Limagne Graben, France*

26 158 The Limagne Graben of the Massif Central Rift (hereafter MCR), France
27 159 experienced three main rifting-related magmatic events (Fig. 1b; Michon
28 160 and Merle, 2001). The first event preceded the formation of the rift basin
29 161 and consisted of very scarce and scattered volcanism affecting a vast area
30 162 comprising the future grabens and their surroundings. The second event
31 163 immediately followed the formation of the graben and produced more than
32 164 200 monogenetic vents scattered in-rift to the North of the MCR, coinciding
33 165 with the areas of pronounced crustal thinning; lastly, the major volcanic

1
2
3
4
5
6
7
8
9
10 166 events mainly contributed to the formation of the Chaîne des Puys, the
11 167 Monts Dore and Sancy stratovolcanoes and the Dèves basaltic shield, which
12
13 168 are all located off-rift from the main graben; the more recent eruptions were
14
15 169 also all confined to the outside of the basin. These latter major volcanic
16
17 170 episodes were also associated with the uplift of the Massif Central, suggesting
18
19 171 a common origin for uplift and volcanism. Michon and Merle (2001) further
20
21 172 noticed that the development of the Eifel and the Ohře Eger rift in the Czeck
22
23 173 Republic followed a nearly identical history, with similar spatio-temporal and
24
25 174 geochemical patterns.

26 27 175 *2.3. Baikal Rift, Russia*

28
29
30 176 Volcanism in the Baikal Rift (hereafter BR), Russia is scarce and almost
31
32 177 exclusively restricted to the flanks of the graben, but some volcanic cen-
33
34 178 ters are present in the Tunka depression (Fig. 1c; Ivanov and Demonterova,
35
36 179 2010). Moreover, a high seismic velocity, high reflectivity anomaly is present
37
38 180 at depth below the rift, which Thybo and Nielsen (2009) attributed to the
39
40 181 presence of multiple strong reflectors in the lower crust, interpreted to be
41
42 182 horizontal sill-like magmatic intrusions. These intrusions would isostatically
43
44 183 compensate the formation of the graben, explaining the lack of crustal thin-
45
46 184 ning observed in the same area.

47 48 185 *2.4. Songliao Graben, China*

49
50 186 Volcanism in the Songliao Graben (hereafter SG), China commenced in
51
52 187 the late Cretaceous with eruption of basalts scattered across the graben floor
53
54 188 and on limited portions of the eastern flank (Fig. 1d; Liu et al., 2001). From
55
56
57
58

1
2
3
4
5
6
7
8
9
10 189 39 to 1.5 Ma, no volcanism has been detected inside the graben, and erup-
11 190 tions have focused on its eastern and western flanks, migrating progressively
12
13 191 further from the graben (Liu et al., 2001). Lastly, the most recent eruptions
14
15 192 (< 0.58 Ma) have clustered on the northwestern margin of the graben and
16
17 193 on the southeastern flank of the basin. Furthermore, high V_p/V_s ratios, high
18
19 194 V_p and regional gravity suggest the presence of mafic intrusions in the lower
20
21 195 crust (He et al., 2014).

22
23
24 196 *2.5. Summary of Observations*

25
26 197 Volcanism in rifts is observed to follow spatio-temporal patterns as the
27
28 198 rift evolves (Fig. 2). Volcanism commonly precedes rift initiation, with vo-
29
30 199 luminous eruptions distributed across a large area eventually comprising the
31
32 200 rift graben and flanks (black stripe in Fig. 2; e.g. Pasteels et al., 1989; Michon
33
34 201 and Merle, 2001; Corti, 2009). Rifting preferentially initiates in zones of in-
35
36 202 herited lithospheric weakness such as suture zones or old faults (Brune et al.,
37
38 203 2023). As extension proceeds, deformation localizes through displacement
39
40 204 on large boundary faults, resulting in the formation of a graben (e.g. Corti,
41
42 205 2009). The latter can be asymmetric (half-graben), symmetric (full-graben),
43
44 206 or transition from one to the other during its lifetime (e.g. Baker et al., 1972).
45
46 207 Volcanism, in turn, localizes inside the graben (blue stripe in Fig. 2; e.g. Liu
47
48 208 et al., 2001; Michon and Merle, 2001; Corti, 2009). Prolonged extension
49
50 209 results in the progressive downthrow of the rift graben along the boundary
51
52 210 faults, and enhanced sedimentation due to the formation of large topographic
53
54 211 gradients. Developed rifts are usually associated with volcanic centers punc-
55
56 212 tuating the graben flanks (purple stripe in Fig. 2; e.g. Liu et al., 2001; Michon
57
58 213 and Merle, 2001; Corti, 2009), and the accumulation of layered magmatic in-

1
2
3
4
5
6
7
8
9
214 intrusions in the crust (Thybo and Nielsen, 2009; Thybo and Artemieva, 2013).
10
215 These intrusions have been observed in a variety of extensional settings and
11
12
216 rift zones, both active and inactive ones (Thybo and Artemieva, 2013), such
13
14
217 as the Baikal Rift, Russia (Thybo and Nielsen, 2009), the East African Rift
15
16
218 System (Birt et al., 1997; Mackenzie et al., 2005), the Rhine Graben, Ger-
17
18
219 many (Wenzel et al., 1991), the Eger Rift, Central Europe (Hrubcová et al.,
19
20
220 2017) the North American Midcontinent Rift (Hinze et al., 1992), the Don-
21
22
221 bas Basin, Ukraine (Lyngsie et al., 2007) and the Songliao Graben, China
23
24
222 (He et al., 2014). Lastly, some rifts achieve maturity, accompanied by the
25
26
223 deactivation of the boundary faults and the localization of volcanism and
27
28
224 deformation in the axial portion of the graben (e.g. Corti, 2009). This marks
29
30
225 the transition to oceanic spreading (e.g. Ebinger and Casey, 2001). Although
31
32
226 the transitions between the so defined phases of magmatic activity occur on
33
34
227 much shorter timescales if compared to the overall duration of rift volcanism,
35
36
228 overlap between different stages is often observed. Changes in melt availabil-
37
38
229 ity between melt-poor and melt-rich rifts impact the abundance of volcanism
39
40
230 but seem to have no effect on their patterns.

231 **3. Modeling Magma Propagation in Rifted Areas**

232 Physics-based models of magma pathways in brittle-elastic rock may be
233 broken down into two separate components (e.g. Neri et al., 2018; Rivalta
234 et al., 2019):

235 i) A model for the stress state of the Earth's crust or lithosphere. The
236 stress tensor at each point in space and time is calculated superposing the rel-
237 evant stress inducing mechanisms, such as gravitational loadings/unloadings,

1
2
3
4
5
6
7
8
9
10
11
12
13
14
15
16
17
18
19
20
21
22
23
24
25
26
27
28
29
30
31
32
33
34
35
36
37
38
39
40
41
42
43
44
45
46
47
48
49
50
51
52
53
54
55
56
57
58
59
60
61
62
63
64
65

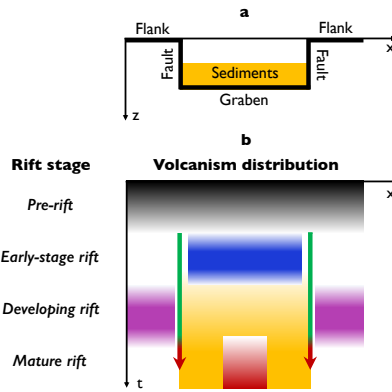


Figure 2: Schematic summary of the observations concerning the spatio-temporal evolution of rift volcanism. **a:** Cross section of a rift showing graben, flanks, sediments and boundary faults. **b:** Timeline showing the mapview distribution of volcanism across the rift. Shaded yellow stripe represents increasing sedimentation. Green- to red-colored arrows represent the progressive deactivation of boundary faults during rift maturity. Colored stripes represent volcanism through the palette used in Figs. 1 and 8.

238 confining and tectonic stresses, and the stresses induced by previous intru-
 239 sions. The stress tensor is then diagonalized at every point in space to obtain
 240 the principal stresses ($\sigma_1, \sigma_2, \sigma_3$ from most compressive to least compressive)
 241 and their orientations. Here we define the vectorial field \vec{v}_3 as having at every
 242 point in space the same orientation as the eigenvector associated to σ_3 and
 243 directed towards the direction where σ_3 is decreasing in magnitude.

244 ii) A model for the trajectories followed by magma in a given stress field.
 245 Such models define a rule for magma propagation that takes as input the
 246 elastic stress field and a starting location for a magma batch, and returns
 247 a magma pathway and an eruptive vent location should the pathway inter-
 248 sect the Earth's surface. The most basic model of magma trajectories was
 249 formulated by Anderson (1937). According to the Anderson theory, faults

1
2
3
4
5
6
7
8
9
250 and dikes have preferred orientations in the field according to their respec-
251 tive dislocation modes. Faults, being shear dislocations, tend to be oriented
252 according to the optimal shearing direction, which is at an angle with respect
253 to the directions of the minimum and maximum principal stresses, depending
254 on friction. In contrast, dikes, needing to open and accommodate a volume,
255 tend to intrude perpendicular to \vec{v}_3 . Following this principle, first-order dike
256 pathways in plane strain configurations can be calculated as lines perpen-
257 dicular to \vec{v}_3 . This method has been used extensively in the literature (e.g.
258 Muller and Pollard, 1977; Pollard, 1987; Roman and Jaupart, 2014; Oliva
259 et al., 2022) and recently extended to three dimensions by Mantiloni et al.
260 (2023). However, this model does not account for the stress induced by the
261 dikes and by their buoyancy. Numerical models that include fracture me-
262 chanics principles (Dahm, 2000; Maccaferri et al., 2010, 2011; Davis et al.,
263 2021) provide more insights by including these additional effects. Princi-
264 pal stress trajectories differ somewhat from those calculated from fracture
265 mechanics principles (Dahm, 2000; Watanabe et al., 2002; Maccaferri et al.,
266 2018).

267 *3.1. A Previous Model for Off-Rift Volcanism*

268 Maccaferri et al. (2014) simulated magma propagation in rifts through
269 the boundary element dike propagation code developed by Maccaferri et al.
270 (2010, 2011) following Dahm (2000). They modeled the state of stress of
271 rift zones by applying a uniform strip-unloading of width W on the free
272 surface of a half-space, simulating the creation of the rift graben. A similar
273 approach based on gravitational unloading had been previously used to model
274 icecap melting (Hooper et al., 2011) and caldera formation (Corbi et al., 2015;

1
2
3
4
5
6
7
8
9
10
11
12
13
14
15
16
17
18
19
20
21
22
23
24
25
26
27
28
29
30
31
32
33
34
35
36
37
38
39
40
41
42
43
44
45
46
47
48
49
50
51
52
53
54
55
56
57
58
59
60
61
62
63
64
65

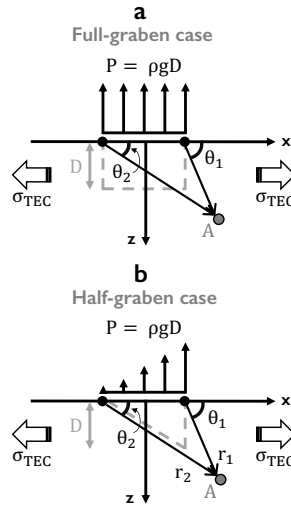


Figure 3: Geometries used for the calculation of stresses in the full-graben (a) and the half-graben (b) cases. Symbols refer to the unloading formulation described in sections 3.1 and 3.3.

Rivalta et al., 2019). The resulting stresses in the elastic half-space are (e.g. Jaeger et al., 2009):

$$\sigma_{zz} = \frac{P}{\pi} [(\theta_1 - \theta_2) - \sin(\theta_1 - \theta_2) \cos(\theta_1 + \theta_2)] \quad (1)$$

$$\sigma_{xx} = \frac{P}{\pi} [(\theta_1 - \theta_2) + \sin(\theta_1 - \theta_2) \cos(\theta_1 + \theta_2)] \quad (2)$$

$$\sigma_{xz} = \frac{P}{\pi} [\sin(\theta_1 - \theta_2) \sin(\theta_1 + \theta_2)], \quad (3)$$

where θ_1 and θ_2 are shown in Fig. 3a, together with the geometry of the system, $P = \rho g D$ is the unloading pressure, ρ is the crustal density, g the acceleration due to gravity and D the basin depth. A uniform stress σ_{tec} was superimposed to simulate tectonic extension.

1
2
3
4
5
6
7
8
9
281 Maccaferri et al. (2014) found that dike trajectories in this problem are
10
11 controlled by the ratio $K = \pi\sigma_{\text{tec}}/2P$ between the tectonic stress and the
12
13 283 unloading pressure: their competition regulates the rotation of the directions
14
15 284 of the principal stresses, which in turn controls the curvature of magma
16
17 285 pathways since dikes propagate roughly perpendicular to the local direction
18
19 286 of least compression \vec{v}_3 . In particular, when the unloading pressure dominates
20
21 287 over the tectonic stretching, \vec{v}_3 becomes vertical or sub-vertical over a depth
22
23 288 interval under the graben. The condition for which \vec{v}_3 is vertical along the z
24
25 289 axis is obtained by requiring that (Maccaferri et al., 2014):

$$\sigma_{zz}(x = 0, z) > \sigma_{xx}(x = 0, z) + \sigma_{\text{tec}} \quad (4)$$

290 since the shear stresses σ_{xz} are null in $x = 0$ (eq. 3). Substituting eqs. 1 and
291 2 in eq. 4, they found that when $K < 1$ the stress barrier is located at depth

$$z_1 < z < z_2 \quad (5)$$

292 where

$$z_1 = \frac{W}{2} \frac{1 - \sqrt{1 - K^2}}{K}, \quad z_2 = \frac{W}{2} \frac{1 + \sqrt{1 - K^2}}{K}. \quad (6)$$

293 As a consequence, dikes ascending from below z_1 are deflected from their
294 vertical path, and if voluminous enough to escape the stress barrier end up
295 reaching the surface outside the graben. Maccaferri et al. (2014) termed
296 ‘stress barrier’ the region between z_1 and z_2 where \vec{v}_3 is subvertical.

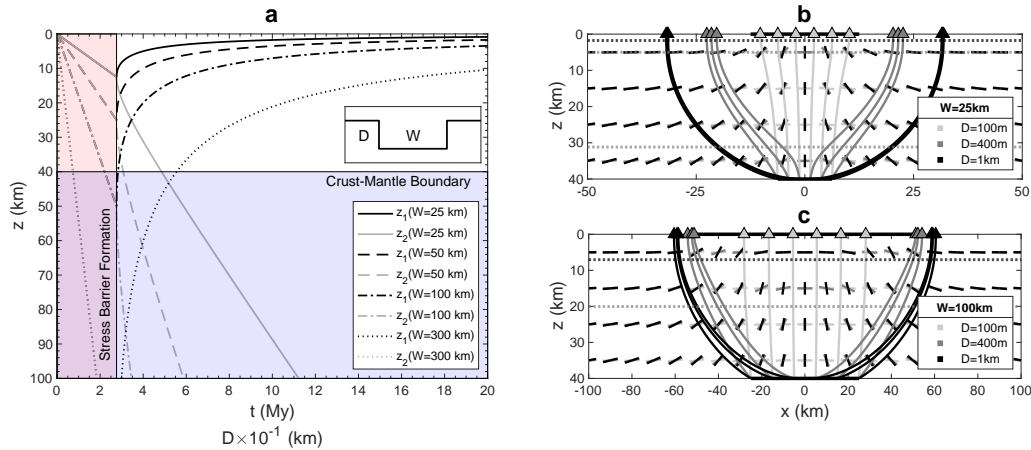


Figure 4: **a**: Evolution of the stress barrier: z_1 (black) and z_2 (gray) for a full-graben deepening at a rate of $\alpha = 1 \times 10^{-4}$ m/y, plotted with respect to time for graben widths $W = 25, 50, 100$ and 300 km. Figure is colored in blue below the chosen depth of the Moho $z_{\text{Moho}} = 40$ km. Figure is colored in red up to the critical depth (or time) of stress barrier formation. Inset shows the geometry of the unloading. **b-c**: Directions of least compression (short segments), dike trajectories (curved lines) and surface arrivals (triangles) in a $W = 25$ km (**a**) and a $W = 100$ km (**b**) wide full-graben for $D = 100$ m (light gray), $D = 400$ m (dark gray) and $D = 1$ km (black). A uniform horizontal tensional stress $\sigma_{tec} = 5$ MPa is superimposed to the unloading stresses. Horizontal lines represent the upper and lower limits of the stress barrier. Black bold segments at $z = 0$ km and $z = 40$ km represent the extent of the rift and the magma ponding zone, respectively.

1
2
3
4
5
6
7
8
9
297 *3.2. Evolution of Rift Stresses Through Time*

10
11 Here, we extended the model of Maccaferri et al. (2014) to a time-
12
13 dependent problem. We employed a plane strain assumption and modeled a
14
15 deepening rift through a gradually increasing strip unloading (eqs. 1-6). The
16
17 strip unloading formulation has the advantage of keeping the model simple
18
19 and transparent and not relying on too many parameters, facilitating the
20
21 interpretation of results. A comparison of the stresses resulting from eqs. 1,
22
23 2 and 3 and numerical boundary element calculations accounting for the con-
24
25 tribution of the shape of the free-surface to the gravitational stresses shows
26
27 that for the geometries relevant here the stress models are similar both in
28
29 terms of orientation and intensity of the principal stresses (Fig. S1); this con-
30
31 firms that the analytical unloading formulas in plane strain are adequate for
32
33 calculating at zero-order the stress induced by a simplified graben geometry.
34
35 Rift basin length along their axis generally exceeds their width and depth
36
37 by at least an order of magnitude, motivating our plane strain assumption,
38
39 which therefore applies to the central parts of the basins and breaks down
40
41 close to their extremities. In order to explore more complex geometries, or
42
43 the behaviour of dikes propagating close to the far ends of the basins or along
44
45 their length, more elaborate 3-D models need to be used (e.g. Davis et al.,
46
47 2021).

48 For simplicity, we assumed that the unloading width W remains constant
49
50 throughout most of the rifting process and that the rift deepens at a constant
51
52 deepening rate α , so that D evolves as $D = \alpha t$. This approximation is
53
54 supported by evidence suggesting that the width of narrow rifts is acquired
55
56 early in their lifetime and does not reflect their age, making fault downthrow
57
58

1
2
3
4
5
6
7
8
9 and sediment infill better indicators of rift maturity (Modisi et al., 2000).

10
11 The time dependent unloading pressure is therefore given by:

$$12 \quad P(t) = \rho g D(t) = \rho g \alpha t, \quad (7)$$

13
14
15
16
17 where P at a given time t is the result of the cumulative downthrow D of the
18 graben up to time t . In other words, it is the existence of the graben that
19 generates the stresses, rather than its deepening velocity.
20
21

22
23 Substituting eq. 7 in eqs 6 we obtained two equations for the time de-
24 pendence of the upper and lower depth of the stress barrier:
25
26

$$27 \quad z_1 = \frac{W}{\pi} \frac{\rho g \alpha t}{\sigma_{tec}} \left(1 - \sqrt{1 - \left(\frac{\pi}{2} \frac{\sigma_{tec}}{\rho g \alpha t} \right)^2} \right) \quad (8)$$

$$28 \quad z_2 = \frac{W}{\pi} \frac{\rho g \alpha t}{\sigma_{tec}} \left(1 + \sqrt{1 - \left(\frac{\pi}{2} \frac{\sigma_{tec}}{\rho g \alpha t} \right)^2} \right). \quad (9)$$

29
30
31
32
33 The evolution of the stress barrier is shown in Fig. 4 for several values of
34 rift width W . We will use these results as an aid to understand our numerical
35 simulations for the full-graben case (see sections 3.4 and 4.1).
36
37

38 39 40 41 42 43 3.3. Half-Graben

44
45 Half-grabens can be modeled in a similar way to full grabens by con-
46 sidering unloading strips shaped as right triangles (Fig. 3b). The resulting
47 stresses in a half-space are (Jaeger et al., 2009, note that here we have fixed
48 a sign mistake):
49
50
51
52

$$53 \quad \sigma_{zz} = \frac{P}{2\pi} [[1 + (x/b)](\theta_1 - \theta_2) - \sin(2\theta_1)] \quad (10)$$

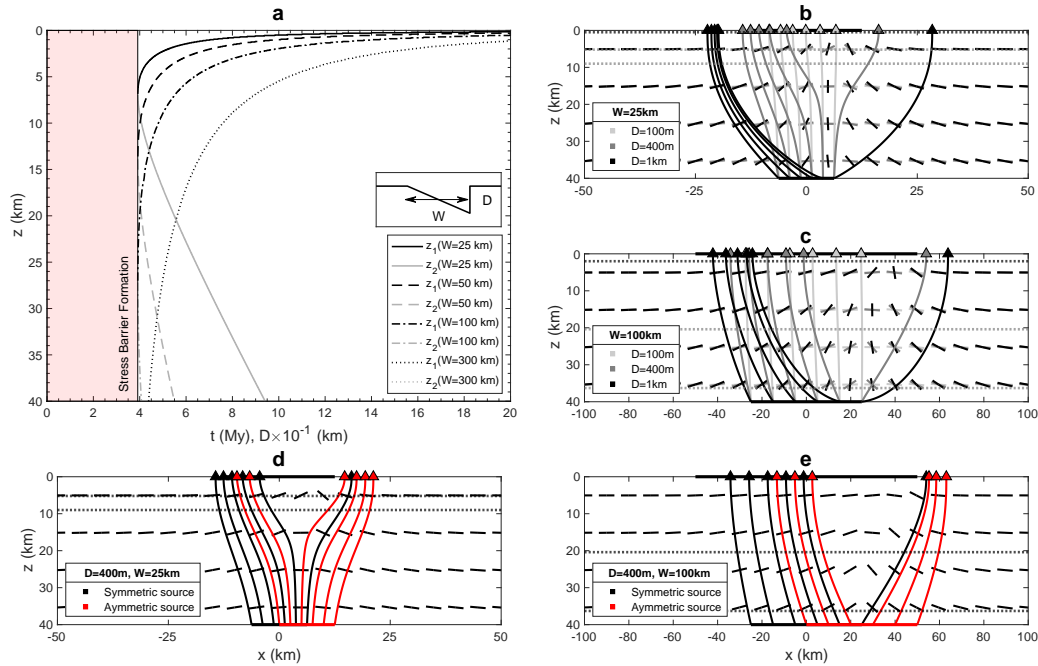


Figure 5: **a**: Evolution of the stress barrier for a half-graben: z_1 (black) and z_2 (gray) for a full-graben deepening at a rate of $\alpha = 1 \times 10^{-4}$ m/y, plotted with respect to time for graben widths $W = 25, 50, 100$ and 300 km. Figure is colored in blue below the chosen depth of the Moho $z_{\text{Moho}} = 40$ km. Figure is colored in red up to the critical depth (or time) of stress barrier formation. Inset shows the geometry of the unloading. **b-c**: Directions of least compression (short segments), dike trajectories (curved lines) and surface arrivals (triangles) in a $W = 25$ km (**a**) and a $W = 100$ km (**b**) wide half-graben for $D = 100$ m (light gray), $D = 400$ m (dark gray) and $D = 1$ km (black). **d-e**: Directions of least compression (short segments), dike trajectories (curved lines) and surface arrivals (triangles) in a $D = 400$ m deep, $W = 25$ km (**d**) and $W = 100$ km (**e**) wide half-graben for a symmetric (black bold lines and triangles) and an asymmetric (red bold lines and triangles) ponding zone. A uniform horizontal tensional stress σ_{tec} is superimposed to the unloading stresses. Horizontal lines represent the upper and lower limits of the stress barrier. Black bold segments at $z = 0$ km and $z = 40$ km represent the extent of the rift and the magma ponding zone, respectively.

$$\sigma_{xx} = \frac{P}{2\pi} [[1 + (x/b)](\theta_1 - \theta_2) + \sin(2\theta_1) - (2z/b) \ln(r_2/r_1)], \quad (11)$$

$$\sigma_{xz} = \frac{P}{2\pi} [1 - (z/b)(\theta_1 - \theta_2) + \cos(2\theta_1)], \quad (12)$$

337 where $b = W/2$ and θ_1, θ_2, r_1 and r_2 are shown in Fig. 3b.

338 We determined the stress barrier by finding the region where the shear
 339 stresses vanish and the direction of least compression \vec{v}_3 is vertical (eq. 4),
 340 that is by solving

$$1 - (z/b)(\theta_1 - \theta_2) + \cos(2\theta_1) = 0 \quad (13)$$

341 and

$$\sigma_{zz}(x_0(z), z) > \sigma_{xx}(x_0(z), z) + \sigma_{tec}, \quad (14)$$

342 where $x_0(z)$ satisfy Eq. 13.

343 We solved eqs. 13 and 14 numerically for different values of D (i.e. for
 344 increasing time), assuming a rift deepening at a constant deepening rate
 345 α , as in the full-graben case (Fig. 5). As in section 3.2, we superimposed
 346 a uniform tectonic extensional stress σ_{tec} . We will use these results as an
 347 aid to compare our numerical simulations for a full-graben to the case of a
 348 half-graben (see sections 3.4 and 4.2).

349 3.4. Numerical Simulations

350 We conducted numerical simulations to understand how the stresses gen-
 351 erated by an evolving graben topography affect the spatio-temporal evolution

1
2
3
4
5
6
7
8
9 352 of rift magmatism in rifts. To do so, (i) we modified the stress model used
10 353 by Maccaferri et al. (2014) to account for the loading generated by sedimen-
11 354 tation within the rift, (ii) and we extended the code developed by Maccaferri
12 355 et al. (2011) to account for the interaction between successive dike intrusions
13 356 in order to apply it to our time-dependent problem.
14
15
16
17
18

19 357 *3.4.1. The Boundary Element Code*

20
21 358 In the original code, growth and propagation of an isolated crack filled
22 359 with a buoyant, inviscid fluid is calculated for any given stress field. The
23 360 dike is modeled as a mixed mode crack, made of a set of contiguous and
24 361 interacting dislocations. The stress boundary conditions are provided by i)
25 362 the magma overpressure, which is the difference between the magma pres-
26 363 sure and the confining stress, the latter resulting from the superposition of
27 364 lithostatic pressure and the normal components of topographic or tectonic
28 365 stresses; and ii) the shear stress due to any tectonic stress or topographic
29 366 load. The trajectory of the dike is determined by adding a new disloca-
30 367 tion ahead of the crack tip, testing different orientations and selecting that
31 368 which maximizes the sum of strain and gravitational energy release (Griffith,
32 369 1921; Dahm, 2000). The emplacement of dikes at depth modifies the local
33 370 stress field: propagation of dikes in the proximity of previously emplaced
34 371 ones results in focusing and crossing of dikes (Ito and Martel, 2002; Kühn
35 372 and Dahm, 2008). We model dike interaction by updating the background
36 373 stress field for subsequent simulations superposing the stress field produced
37 374 by previously emplaced dikes. Dikes that reach the surface of the modeled
38 375 half-space are assumed to erupt, their stress field is not considered in the
39 376 following computations.
40
41
42
43
44
45
46
47
48
49
50
51
52
53
54
55
56
57
58

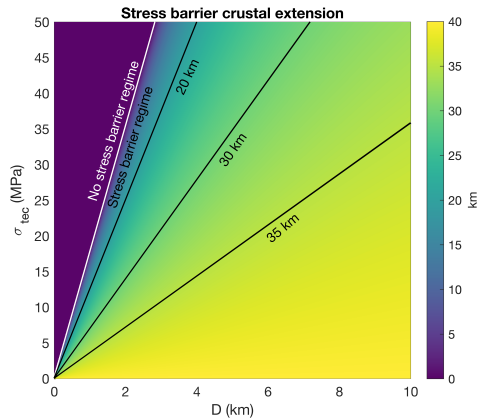


Figure 6: Extension of the stress barrier in a 40 km deep crust as a function of basin depth D and tectonic extensional stress σ_{tec} . White line represents the transition from the "no stress barrier regime" to the "stress barrier regime". Black lines are isopleths of stress barrier crustal extension.

377 The effective unloading pressure at any time is given by

$$P_{\text{eff}}(t) = g[\rho D(t) - \rho_s T(t)] \quad (15)$$

378 where ρ_s is the density of the sediments.

379 3.4.2. Model Parameters and Setup

380 We assumed the background state of stress σ^b to be lithostatic, so that
 381 $\sigma_{xx}^b(z) = \sigma_{zz}^b(z) = \rho g z$ and we superimposed to the unloading stresses cal-
 382 culated from eqs. 1, 2 and 3 a uniform tectonic extensional stress $\sigma_{\text{tec}} = 5$
 383 MPa, in line with the choice of Maccaferri et al. (2014). Regional and tectonic
 384 stresses in the crust and lithosphere build up until they match the stresses
 385 at which rock is expected to yield. Previous works have estimated the total
 386 force exerted by tectonic processes (ridge push, slab pull) on the lithosphere
 387 to be approximately $1 - 4 \text{ TN m}^{-1}$ (e.g. Forsyth and Uyeda, 1975; Kuszniir,

1
2
3
4
5
6
7
8
9
388 1991), and this has been repeatedly assumed to represent the strength of
10
389 the lithosphere (Liu and Zoback, 1997; Zoback and Townend, 2001). For a
11
12 the lithospheric thickness of 100 km, this would imply a strength of 10 – 40 MPa.
13
390
14
391 Laboratory experiments and numerical models have constrained the strength
15
16 of cratonic lithosphere to be of the order of 100 MPa (Kohlstedt et al., 1995;
17
18 Mallard et al., 2016). However, rifting initiation preferentially occurs along
19
20 lithospheric suture zones where continents collided during previous stages
21
22 of the Wilson cycle (Brune et al., 2023). For instance, this is the case for
23
24 the Afro-Arabian Rift System (Corti, 2009), the Baikal Rift (Logatchev and
25
26 Zorin, 1992) and the Massif Central Rift (Faure et al., 2009). Suture zones
27
28 are much different from those of cratons due to inherited weaknesses and the
29
30 presence of a thickened and hotter crust, with the net result of making them
31
32 weaker and therefore preferential sites of strain localization (Brune et al.,
33
34 2023). In fact, the strength of suture zones is considered to be at least a fac-
35
36 tor of 10 less than that of cratons (Hyndman et al., 2005), resulting in yield
37
38 stresses of the order of 10 MPa, as applied by previous numerical models
39
40 (Dang et al., 2020). This is a factor of 2 greater than our chosen parameter.
41
42 However, the key parameter in our models is not the extensional stress itself,
43
44 but the ratio $K = \pi\sigma_{\text{tec}}/2P$ between the latter and the unloading pressure
45
46 (Fig. 6). Consequently, higher tectonic stresses can result in the same pat-
47
48 tern provided that K stays constant (that is if deeper basins are considered),
49
50 which is the case for many existing rifts. For instance, the Limagne graben
51
52 of the French Massif Central Rift is at least 3 km deep, grabens in the Main
53
54 Ethiopian Rift and in the Kenya Rift are up to 5 km deep, while the Baikal
55
56 Rift graben reaches depths of 10 km.
57
58
59
60
61
62
63
64
65

1
2
3
4
5
6
7
8
9
413 We conducted 20 sets of simulations for a $W = 100$ km wide full graben
10
414 (Fig. 8). All the physical parameters employed in the simulations are listed in
11
12
13
415 Table 1. During the first 10 sets the graben deepens from $D = 100$ m to $D =$
14
416 1 km at steps of 100 m each. For the remaining 10 sets, we account for the
15
16
417 role of sedimentation through the superposition of a strip loading increasing
17
18
418 from a thickness of $T = 100$ m to $T = 800$ m, reflecting the progressive
19
20
419 leveling of topographic gradients in rifts operated by sedimentation. For
21
22
420 simplicity, during sedimentation, the basin depth was kept fixed at $D = 1$
23
24
421 km, simulating the deactivation of the boundary faults during rift maturity.
25
26
422 This assumption has the advantage of isolating the effect of sedimentation,
27
28
423 favoring a clearer interpretation of the results of our idealized model. In
29
30
424 reality, graben deepening and sedimentation rates are expected to proceed in
31
32
425 parallel during rift evolution and are not expected to be entirely independent.

33
34
426 After each deepening/sedimentation step, we injected a group of dikes
35
36
427 (ranging from 4 during the first sets to 8 during the last) from depth and let
37
38
428 them propagate until they either reached the surface or stalled. Each dike
39
40
429 was injected after the propagation of the previous dike had ceased. If the
41
42
430 dike reaches the surface, it is assumed to erupt, and its stress field is not
43
44
431 considered in the computation of the background stress for the subsequent
45
46
432 dikes. If the dike stalls in the crust, we add the stress field generated by the
47
48
433 dike after its emplacement to the background stress, and let the following
49
50
434 dikes propagate in the updated stress field. A flow chart illustrating the
51
52
435 numerical simulations is provided in Fig. 7

53
436 Each injected dike has a magma density at atmospheric pressure of 2600 kg/m^3 .
54
55
437 Less buoyant magmas would require more volume to propagate (Weert-

1
2
3
4
5
6
7
8
9
10
11
12
13
14
15
16
17
18
19
20
21
22
23
24
25
26
27
28
29
30
31
32
33
34
35
36
37
38
39
40
41
42
43
44
45
46
47
48
49
50
51
52
53
54
55
56
57
58
59
60
61
62
63
64
65

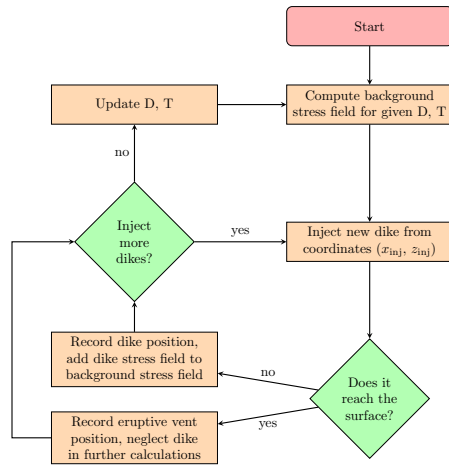


Figure 7: Flow chart illustrating the workflow of the numerical simulations.

man, 1971; Secor Jr and Pollard, 1975). For the first sets of simulations, dikes were injected from a depth representing the crust-mantle boundary ($z_{inj} = z_{Moho} = 40$ km). Over the suite of simulations, we increased the number of injected dikes to represent intensified melting due to decompression of the asthenosphere, and we progressively changed the injection depth z_{inj} following the emplacement of progressively shallower crustal intrusions that can act as new locations of dike nucleation ($z_{inj} < z_{Moho}$). The horizontal injection coordinate x_{inj} was also progressively changed to reflect higher probabilities of dike nucleation from areas of higher sill density. Detailed input parameters for the model setup of each set of simulations, including basin depth, sediments thickness, and starting location of every dike are provided in Table S1.

Table 1: Values of the parameters employed in the simulations

Symbol	Definition	Value or Range	Unit
D	Basin depth	0-1000	m
D_c	Basin depth at stress barrier formation ($D_c = \pi\sigma_{tec}/2\rho g$)	280	m
g	Gravitational acceleration	9.81	m·s ⁻²
K	Magma bulk modulus	10	GPa
l	Initial dike length	5	km
l_0	Elementary dislocation length	0.1	km
P	Unloading pressure ($P = \rho g D$)	28	MPa
T	Sediment thickness	0-800	m
t_c	Time at stress barrier formation ($t_c = \pi\sigma_{tec}/2\rho g\alpha$)	2.8	Myr
V	Dike cross-sectional area	0.0075	km ²
W	Graben width	25, 50, 100	km
α	Graben deepening rate	1×10^{-4}	m·yr ⁻¹
ρ_m	Magma density	2600	kg·m ⁻³
z_1	Upper limit of the stress barrier	-	m
z_2	Lower limit of the stress barrier	-	m
z_{inj}	Dike injection depth	40-24	km
z_{Moho}	Crust-Mantle boundary depth	40	km
ρ_m	Magma density	2600	kg·m ⁻³
μ	Rock rigidity	20	GPa
ρ	Rock density	2900	kg·m ⁻³
ρ_s	Sedimentary layer density	2700	kg·m ⁻³
σ_{tec}	Extensional uniform tectonic stress	5	MPa

1
2
3
4
5
6
7
8
9 450 **4. Results**

10
11 451 *4.1. Time Evolution of Rift Volcanism*

12
13
14 452 From our simulations, we identify four main stages in the development of
15
16 453 rift-related volcanism:

17
18 454 i) Early in-rift volcanism: as long as $D < D_c = \pi\sigma_{tec}/2\rho g\alpha$, the basin is
19
20 455 not deep enough for a stress barrier to form and the real parts of eqs 8 and
21
22 456 9 coincide (Fig. 4a). During this regime the direction of least compression
23
24 457 is roughly horizontal everywhere below the graben (Fig. 4c), so that dikes
25
26 458 ascend sub-vertically towards the surface of the basin (Fig. 8a). Trajectories
27
28 459 tend to diverge from each other so that dike eruptions are scattered across
29
30 460 the rift depression during this first stage.

31
32 461 ii) Off-rift volcanism and sills emplacement: as the basin deepens, the
33
34 462 unloading pressure grows to eventually overcome the tectonic stresses, so that
35
36 463 \vec{v}_3 becomes vertical under the rift in a zone bounded by z_1 and z_2 , creating a
37
38 464 stress barrier (Fig. 4). This happens for the critical depth $D_c = \pi\sigma_{tec}/2\rho g$,
39
40 465 which is independent of rift width. In our case, this critical depth is about
41
42 466 280 m. Ascending dikes are deflected towards the flanks of the depression,
43
44 467 shifting the pattern to off-rift eruptions. After the nucleation of the stress
45
46 468 barrier, dike trajectories become increasingly more tightly spaced as the rift
47
48 469 deepens, reducing the distance between surface arrivals and promoting the
49
50 470 formation of a few large polygenetic volcanic edifices.

51
52 471 The stress barrier then broadens with time, with z_1 slowly approaching
53
54 472 the surface while z_2 quickly descends to depth (Fig. 4a). Also, for wider
55
56 473 rifts, or as rifts get wider, the stress barrier forms at greater depths and
57
58 474 grows faster. This is because z_1 and z_2 scale with rift width (eqs 8, 9). As

1
2
3
4
5
6
7
8
9
10 475 a consequence, the barrier already extends beneath the Moho shortly after
11 476 it has formed for rifts as wide as $W = 50$ km and forms in the lithospheric
12
13 477 mantle, in this example, for $W > 85$ km.

14
15 478 iii) Piling up of stacked sills and off-rift volcanism: if the stress barrier
16
17 479 comprises the dike injection depth (i.e. if $D > \pi\sigma_{\text{tec}}/2\rho g$, and $z_{\text{inj}} > z_1$),
18
19 480 dikes injected close to the rift axis may be deviated into horizontal sill-like
20
21 481 structures. Due to their very limited vertical extent, they may then lack
22
23 482 the buoyancy needed to propagate and remain trapped in the lower crust
24
25 483 (Fig. 8b). These horizontal intrusions can in turn collect melt supplied by
26
27 484 further injections from below and serve as magma ponding zones from where
28
29 485 subsequent dikes are nucleated. This way, progressively shallower horizontal
30
31 486 intrusions form, promoting the stacking of the sills under the rift (Fig. 8c).

32
33 487 iv) Late in-rift volcanism: over long time scales the stacked sills may
34
35 488 intrude thick portions of the crust so that z_{inj} approaches z_1 . Concurrently, in
36
37 489 our simulations, the sedimentation rate exceeds the deepening rate, reflecting
38
39 490 deactivation of the boundary faults during rift maturity. As a result, the
40
41 491 loading due to the accumulation of sediments progressively compensates the
42
43 492 unloading induced by the excavation of the rift, causing z_1 to deepen and
44
45 493 eventually overcome z_{inj} . When z_{inj} coincides with z_1 , the shallowest possible
46
47 494 sill is created at a depth of about z_1 . Above this depth, the direction of
48
49 495 least compression is horizontal again so that dikes injected from the sill at
50
51 496 the top of the pile erupt inside the rift basin. The combined effect of the
52
53 497 shallowing of the injection depth due to sill stacking and the deepening of
54
55 498 the stress barrier due to sedimentation, thus, promotes a later stage where
56
57 499 volcanism shifts back to the inside of the rift (Fig. 8d). A dike nucleating

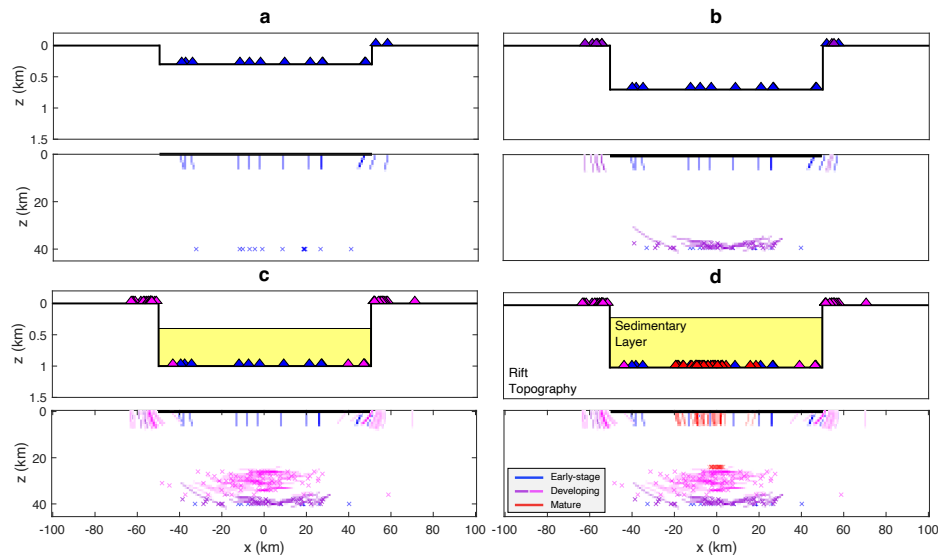


Figure 8: **a-d**: The four stages of rift-related volcanism identified in our simulations. **a**: Early scattered in-rift volcanism. **b**: Off-rift volcanism and sill formation. **c**: Sill stacking and off-rift volcanism. **d**: Late axial in-rift volcanism. *Upper panels*: Bold line represents rift topography. Sedimentary layer is patched in yellow. Colored triangles mark the locations of surface dike arrivals. *Lower panels*: Density plots of dike emplacements. Colored crosses indicate the coordinates at which dikes are injected.

from this shallow depth is expected to be oriented vertically (see orientation of principal stresses above z_1 in Fig. 4b) and propagate laterally along the rift axis. Thus, stress-driven dikes in this phase may dislocate at once the entire layer of crust above the stacked sills and create the conditions for more focused crustal splitting and dike propagation, representing a shift from continental rifting to incipient oceanic spreading.

4.2. Comparison With a Half-Graben

Half-grabens require a larger basin depth to develop a stress barrier, and for a given graben depth, a half-graben stress barrier locates at a shallower

1
2
3
4
5
6
7
8
9
10
11
12
13
14
15
16
17
18
19
20
21
22
23
24
25
26
27
28
29
30
31
32
33
34
35
36
37
38
39
40
41
42
43
44
45
46
47
48
49
50
51
52
53
54
55
56
57
58
59
60
61
62
63
64
65

509 depth, if compared to a full-graben (Figs. 4a and 5a). The first of these dif-
510 ferences has the effect of extending the period of time during which there is
511 no stress barrier, promoting a longer phase of monogenetic scattered volcan-
512 ism inside the rift basin. The second difference, in turn, results in prolonging
513 the time (and depth) interval for which $z_1 < z_2 < z_{\text{Moho}}$, favoring dike ascent
514 and reducing the likelihood of sill formation.

515 The shear stresses σ_{xz} for a rectangular basin are null only for $x = 0$, so
516 that the stress barrier sits below the rift axis (Maccaferri et al., 2014). The
517 stress barrier for the half-graben has a different shape, being shifted to the
518 right of $x = 0$ and deflected towards the deeper side of the graben (Fig. 5).
519 The main consequence is that dike trajectories are no longer symmetrical
520 with respect to $x = 0$. Assuming that dikes are injected from a horizontal
521 strip of length $W/2$ centered at $x = 0$ (as in the full graben case), this
522 results in more concentrated paths on the negative x direction. The resulting
523 volcanism would therefore tend to focus on the left side of the half-graben,
524 that is its shallowest part (Fig. 5d,e). However, magma trajectories and
525 the resulting surface arrivals for a half-graben are strongly sensitive to the
526 horizontal coordinate at which dikes nucleate: dikes injected from below the
527 shallower side of the basin may still erupt within the rift, while those that
528 form under the deeper side tend to ascend towards the flank. If the deep
529 magma ponding zone is shifted towards the deeper side (e.g. in a hypothesis
530 where the decompression due to the graben formation contributes to melting)
531 more trajectories will come from the deeper side of the basin, favoring off-rift
532 arrivals or even one-sided volcanism (Fig. 5d,e).

533 As the barrier grows both in extension and intensity, surface volcanism

1
2
3
4
5
6
7
8
9
534 becomes less scattered and tends to concentrate in narrower areas, as was
10
11 535 also observed in the the full-graben case. In this case, however, the presence
12
13 536 of the stress barrier does not hinder the possibility of in-rift volcanism on the
14
15 537 shallower side of the basin, even for high values of basin depth D .

18 538 **5. Discussion**

20
21 539 We showed that as a deepening rift graben progressively decompresses
22
23 540 the crust and lithosphere, decompression is accompanied by a gradual rota-
24
25 541 tion of crustal stresses. If the graben becomes deeper than a critical depth,
26
27 542 the magnitude of the stress rotation can be locally so large that the most
28
29 543 and least compressive stress directions may switch. Since magma pathways
30
31 544 are predominantly steered following the orientation of principal stresses, a
32
33 545 deepening rift may be associated by significant shifts in the distribution of
34
35 546 surface vents and in the architecture of crustal intrusions, with a predomi-
36
37 547 nantly vertically-organized fabric switching to underplating.

38 548 The same principles that we employed in our work have been used with
39
40 549 growing success to estimate the propagation pathways of magma at the vol-
41
42 550 cano scale in several different settings (e.g. Hooper et al., 2011; Roman and
43
44 551 Jaupart, 2014; Sigmundsson et al., 2015; Rivalta et al., 2019). This further
45
46 552 supports our simple model.

47
48 553 On the basis of the success of this extremely simplified approach (com-
49
50 554 pared to the complexity and number of parameters of a geodynamic model)
51
52 555 we propose that the main features of magmatism and volcanism in rifts and
53
54 556 elsewhere can be reproduced by accounting for a few factors: 1) elasticity
55
56 557 (as described by Hooke's law), 2) gravitational stresses due to redistribution

1
2
3
4
5
6
7
8
9
10
11
12
13
14
15
16
17
18
19
20
21
22
23
24
25
26
27
28
29
30
31
32
33
34
35
36
37
38
39
40
41
42
43
44
45
46
47
48
49
50
51
52
53
54
55
56
57
58
59
60
61
62
63
64
65

558 of surface loads during rift development, 3) dike-dike interactions, 4) phys-
559 ically sound magma pathways calculations that consider dikes as opening
560 fractures, thus aligning perpendicular to \vec{v}_3 . We propose that incorporat-
561 ing our approach into geodynamic models will allow to better constrain how
562 much and where melt volumes are available and the evolution of magma
563 properties, and developing comprehensive geodynamic simulations able to
564 reproduce the main features of magmatism and volcanism. This would in
565 turn provide a way of estimating poorly constrained rifting parameters such
566 as tectonic stresses, which cannot be directly determined (e.g. by using the
567 inversion approaches proposed by Rivalta et al., 2019), and applying our
568 model to specific case studies .

569 *5.1. Comparison With Nature*

570 The broad-scale magmatism and volcanism patterns usually observed dur-
571 ing rift evolution are consistent with our simple analytical stress model, which
572 has only three parameters. The early-stage flankward migration of volcanism
573 is typical of several rifted areas, such as the Main Ethiopian Rift (Chernet
574 et al., 1998; Bonini et al., 2005), the Massif Central Rift (Michon and Merle,
575 2001) and the Songliao Graben (Liu and Zoback, 1997). In our model, the
576 shift occurs once a critical basin depth is reached, which depends on the
577 tectonic extensional stress and the density of the crustal rocks. The current
578 available data do not allow to prove the existence of such a critical depth,
579 but future work can focus on estimating this quantity for rifts of different
580 nature.

581 The emplacement of stacked, sub-horizontal sills in the lower crust or
582 lithospheric mantle is observed ubiquitously across a large number of rift

1
2
3
4
5
6
7
8
9 583 settings (Thybo and Artemieva, 2013). In our model, this is a consequence of
10 584 the stress barrier extending below the dike injection depth, and the resulting
11 585 shallowing of the injection depth as magma progressively pools at shallower
12 586 levels. This may eventually result in dikes nucleating above the stress barrier
13 587 created by rift unloading and erupting in the axial part of the graben. The
14 588 inward migration of volcanism associated with this last phase is commonly
15 589 observed in more mature rifts (such as the MER), where it is crucial in
16 590 assisting the transition to seafloor spreading (e.g. Corti, 2009; Ebinger and
17 591 Casey, 2001).

18 592 While some features of rift magmatism (such as the presence of off-rift
19 593 volcanoes and stacked sills in the middle-lower crust) are common to all
20 594 the natural settings shown in this work, others are not. For example, while
21 595 the MER, the MCR and the SG all exhibit an early flankward migration of
22 596 volcanism, the BR is mostly characterized by off-rift volcanism, with limited
23 597 amount of in-rift volcanics. Moreover, both the SG and the MER showcase
24 598 a late-stage riftward migration of volcanism, but the MCR and the SG do
25 599 not. The model described in this paper is intended not only to provide a
26 600 framework to explain the commonalities between natural settings, but also
27 601 to account for possible differences once the model will be applied in more
28 602 detail to specific case studies.

29 603 *5.2. The Impact of Tectonics*

30 604 The evolution of rift volcanism has been often explained in terms of the
31 605 impact of tectonics on rifting. Frequent explanations argue that as deep-
32 606 reaching boundary faults are established, they would channelize the ascend-
33 607 ing magma and lead to the creation of large volcanoes close to the fault

1
2
3
4
5
6
7
8
9
608 margins (Bosworth, 1987; Ebinger, 1989; Corti et al., 2004). Indeed, off-axis
10
609 volcanoes are often aligned to the boundary faults, suggesting a connection.
11
12
13
610 However, eruptive centers are most frequently located on the footwall of the
14
611 boundary faults and, thus, clearly offset from the suggested magma pathway.
15
16
612 The graben-unloading model offers a simple explanation of the alignments:
17
18
613 the establishment of a graben topography leads magma trajectories starting
19
20
614 from the crust-mantle boundary to converge just off-rift (Maccaferri et al.,
21
22
615 2015; Neri et al., 2018). In the model presented here, we clarify that such
23
24
616 alignments are related to the border faults reaching a critical cumulative
25
26
617 downthrow, and are suppressed once the system of stacked sills beneath the
27
28
618 graben reaches a critical depth.

31 619 *5.3. Limitations of the Model*

32
33
620 Our model does not simulate some rifting-related processes that are usu-
34
35
621 ally accounted for in more complex geodynamical models. In particular, we
36
37
622 consider only brittle-elastic rheology, which is appropriate for dike propaga-
38
39
623 tion, a process occurring on a short time scale of hours to weeks. Seismic
40
41
624 evidence shows that a strong mid-lower crust is present below young rifts
42
43
625 (Déverchère et al., 2001; Craig et al., 2011). The presence of a strong crust
44
45
626 below rifts is also supported by topographies of wavelengths up to hundreds
46
47
627 of kilometers lasting tens of millions of years, which imply the existence of
48
49
628 a thick layer behaving rigidly over the same timespan (Turcotte, 1979). We
50
51
629 note that dike propagation is a viable mechanism for magma transport also
52
53
630 in a visco-elastic material, provided that the viscosity contrast between the
54
55
631 rock and the magma is larger than $10^{11} - 10^{14}$, which is generally true for
56
57
632 basaltic magmas and low-viscosity rhyolitic magmas (Rubin, 1993). In fact,

1
2
3
4
5
6
7
8
9
633 magmatic underplating under continental rifts often occurs through the em-
10
634 placement of sills (Thybo and Nielsen, 2009; Thybo and Artemieva, 2013),
11
12
635 meaning that magma is still able to move by hydraulic fracturing in the lower
13
14
636 crust. Our model does not account for the actual processes that lead to the
15
16
637 formation of a rift graben and its sedimentary infill, which are the result of
17
18
638 the coupled action of extension, erosion and sedimentation over million of
19
20
639 years, while they are imposed as an input in our model. Moreover, regional
21
22
640 tectonic stresses exert primary controls on the deepening rate of a rift, af-
23
24
641 fecting in turn the rate at which rift shoulders are eroded and sediments
25
26
642 deposited inside the graben. Since tectonic stresses can vary in space and
27
28
643 time in rift settings, following changes in the thermal and mechanical state of
29
30
644 the lithosphere, complex feedbacks between the structural features of a rift
31
32
645 and its sedimentation patterns are expected to take place. However, tectonic
33
34
646 stresses, deepening rate and sedimentation rate have been assumed to be
35
36
647 constant and independent in our model. Future applications to specific rifts
37
38
648 will have to account for more accurate formulations.

39
40
649 In our model, melt is assumed to be available from the very beginning of
41
42
650 the rifting process. This is in reality likely true only for magma-rich rifts,
43
44
651 while in magma-poor rifts a minimum stretching factor and, thus, graben
45
46
652 depth would be required for melting to start. Inhibited melt production
47
48
653 during rift initiation could result in preventing the early phase of in-rift
49
50
654 volcanism, essentially skipping or reducing the duration of the first stage of
51
52
655 our results but without affecting the subsequent pattern of magmatism.

53
54
656 Prolonged extension in rifts can result in the shallowing of the Moho due
55
56
657 to crustal thinning (Ruppel, 1995). Alternatively, crustal thickness during
57
58

1
2
3
4
5
6
7
8
9 658 extension can be maintained through the emplacement of sill-like horizon-
10 659 tal magma bodies in the lower crust (Thybo and Nielsen, 2009; Thybo and
11 660 Artemieva, 2013). In our simulations, the evolving geometry of the basin
12 661 controls the emplacement of sills below the rift, which in turn is expected to
13 662 control the amount of Moho uplift required to obtain isostatic equilibrium.
14 663 As a result, lower crustal viscous processes such as Moho uplift are controlled
15 664 top-down in our model by the shallow brittle deformation caused by graben
16 665 formation, with significant implications for rifting dynamics. Implementing
17 666 sound magma propagation principles in geodynamic models could help shed
18 667 light on the dynamics controlling the competition between Moho uplift and
19 668 the emplacement of lower crustal intrusions.

20
21
22
23
24
25
26
27
28
29
30 669 While our current model does not address the petrological aspects of rift
31 670 volcanism, we expect that the different stages envisioned by our model, cor-
32 671 responding to different depths and timescales of stagnation of magma in the
33 672 crust, should leave a detectable signature on the petrology of the erupted
34 673 lavas and released gases. As an example, dike velocity is proportional to the
35 674 square of the driving pressure gradient (Davis et al., 2023), so that dikes
36 675 propagating at an angle δ from the vertical are a factor $\sin^2 \delta$ slower than
37 676 vertically propagating dikes. This results in higher residence time of magma
38 677 in the crust, with significant effects on composition that can be further scru-
39 678 tinized in future studies on the subject.

30 679 **6. Conclusions**

31
32
33
34 680 In spite of its simplifications, our model captures the main features of
35 681 how the distribution of volcanism shifts over time while the rift matures. The
36
37
38

1
2
3
4
5
6
7
8
9
682 main implication of our results is that the evolution of the stresses generated
10
683 by a developing rift basin can account alone for the major aspects of the
11
12
684 spatio-temporal evolution of rift magmatism. Our results imply that most of
13
14
685 these common features may solely depend on the top-down and remote driv-
15
16
686 ing factors considered in our model, that is gravitational stresses due to an
17
18
687 evolving graben topography and tectonic extension, and largely disentangled
19
20
688 from bottom-up factors such as the mechanisms underlying rift initiation,
21
22
689 which would still be important in determining the locations that dikes are
23
24
690 released from. The strong connection between the structural evolution of
25
26
691 a rift and its magmatism therefore motivates a more holistic approach in
27
28
692 collecting data, analyzing and modeling them: joint constraints on the mag-
29
30
693 matic, tectonic and sedimentary history of rifts can help test our hypothesis,
31
32
694 while improvements in the model used here can make it suitable for applica-
33
34
695 tions to specific rifts. Further works on the topic shall also improve the stress
35
36
696 model used here by allowing for spatially and temporally variable tectonic
37
38
697 stresses, more complex graben geometries and crustal density structures and
39
40
698 by including a model of the thermal evolution of the system.

699 **Data availability**

700 The Fortran90 code used for the numerical dike simulations and the in-
701 structions on how to compile and run the code will be made available upon
702 request. All the data used as input for the simulations are attached as sup-
703 porting information.

1
2
3
4
5
6
7
8
9 704 **Acknowledgements**

10
11 705 We are grateful to Richard F. Katz, Derek Keir and two anonymous
12
13 706 reviewers for providing us with valuable comments that greatly improved our
14
15 707 manuscript. This research was funded by the German Research Foundation
16
17 708 (DFG), Grant 634756, RI 2782/2.
18
19
20

21 709 **Appendix A. Supplementary material**

22
23 710 A figure showing the comparison between the analytical unloading for-
24
25 711 mulas used in our model and a boundary element code is provided as supple-
26
27 712 mentary information, together with a table gathering the input data for the
28
29 713 numerical simulations. Supplementary material related to this article can be
30
31 714 found at the online version of the manuscript.
32
33
34

35 715 **References**

- 36
37 716 Anderson, E., 1937. Cone-sheets and ring-dykes: the dynamical explanation.
38
39 717 *Bulletin Volcanologique* 1, 35–40.
40
41
42 718 Baker, B.H., Mohr, P.A., Williams, L.A.J., 1972. *Geology of the Eastern*
43
44 719 *Rift System of Africa*. volume 136. Geological Society of America.
45
46
47 720 Birt, C., Maguire, P., Khan, M., Thybo, H., Keller, G.R., Patel, J., 1997. The
48
49 721 influence of pre-existing structures on the evolution of the southern Kenya
50
51 722 Rift Valley—evidence from seismic and gravity studies. *Tectonophysics*
52
53 723 278, 211–242.
54
55
56
57
58

- 1
2
3
4
5
6
7
8
9 724 Bjorklund, T., Burke, K., Zhou, H.w., Yeats, R.S., 2002. Miocene rifting
10 in the Los Angeles basin: Evidence from the Puente Hills half-graben,
11 725 volcanic rocks, and P-wave tomography. *Geology* 30, 451–454.
12 726
13
14
15 727 Bonini, M., Corti, G., Innocenti, F., Manetti, P., Mazzarini, F., Abebe, T.,
16 728 Pecskey, Z., 2005. Evolution of the Main Ethiopian Rift in the frame of
17 729 Afar and Kenya rifts propagation. *Tectonics* 24.
18
19
20
21
22 730 Bosworth, W., 1987. Off-axis volcanism in the Gregory Rift, East Africa:
23 731 Implications for models of continental rifting. *Geology* 15, 397–400.
24
25
26
27 732 Brune, S., Kolawole, F., Olive, J.A., Stamps, D.S., Buck, W.R., Buiter,
28 733 S.J., Furman, T., Shillington, D.J., 2023. Geodynamics of continental rift
29 734 initiation and evolution. *Nature Reviews Earth & Environment* 4, 235–253.
30
31
32
33 735 Chernet, T., Hart, W.K., Aronson, J.L., Walter, R.C., 1998. New age con-
34 736 straints on the timing of volcanism and tectonism in the northern Main
35 737 Ethiopian Rift–southern Afar transition zone (Ethiopia). *Journal of Vol-
36 738 canology and Geothermal Research* 80, 267–280.
37
38
39
40
41
42 739 Corbi, F., Rivalta, E., Pinel, V., Maccaferri, F., Bagnardi, M., Acocella, V.,
43 740 2015. How caldera collapse shapes the shallow emplacement and transfer
44 741 of magma in active volcanoes. *Earth and Planetary Science Letters* 431,
45 742 287–293.
46
47
48
49
50
51 743 Corti, G., 2009. Continental rift evolution: from rift initiation to incipient
52 744 break-up in the Main Ethiopian Rift, East Africa. *Earth-Science Reviews*
53 745 96, 1–53.
54
55
56
57
58
59
60
61
62
63
64
65

- 1
2
3
4
5
6
7
8
9
10 746 Corti, G., Bonini, M., Sokoutis, D., Innocenti, F., Manetti, P., Cloetingh, S.,
11 747 Mulugeta, G., 2004. Continental rift architecture and patterns of magma
12 migration: A dynamic analysis based on centrifuge models. *Tectonics* 23.
13 748
14
15
16 749 Craig, T., Jackson, J., Priestley, K., McKenzie, D., 2011. Earthquake distri-
17 bution patterns in Africa: their relationship to variations in lithospheric
18 750 and geological structure, and their rheological implications. *Geophysical*
19 751 *Journal International* 185, 403–434.
20
21 752
22
23
24 753 Dahm, T., 2000. Numerical simulations of the propagation path and the ar-
25 rest of fluid-filled fractures in the Earth. *Geophysical Journal International*
26 754 141, 623–638.
27
28 755
29
30
31 756 Dang, Z., Zhang, N., Li, Z.X., Huang, C., Spencer, C.J., Liu, Y., 2020. Weak
32 orogenic lithosphere guides the pattern of plume-triggered supercontinent
33 757 break-up. *Communications Earth & Environment* 1, 51.
34
35 758
36
37
38 759 Davis, T., Bagnardi, M., Lundgren, P., Rivalta, E., 2021. Extreme curvature
39 of shallow magma pathways controlled by competing stresses: insights
40 760 from the 2018 Sierra Negra eruption. *Geophysical Research Letters* 48,
41 761 e2021GL093038.
42
43 762
44
45
46 763 Davis, T., Rivalta, E., Smittarello, D., Katz, R.F., 2023. Ascent rates of
47 3-D fractures driven by a finite batch of buoyant fluid. *Journal of Fluid*
48 764 *Mechanics* 954, A12.
49
50 765
51
52
53 766 Déverchère, J., Petit, C., Gileva, N., Radziminovitch, N., Melnikova, V.,
54 San’Kov, V., 2001. Depth distribution of earthquakes in the Baikal Rift
55 767
56
57
58
59
60
61
62
63
64
65

- 1
2
3
4
5
6
7
8
9
768 System and its implications for the rheology of the lithosphere. *Geophysical*
10
769 *Journal International* 146, 714–730.
11
12
13
14 770 Ebinger, C., Casey, M., 2001. Continental breakup in magmatic provinces:
15
771 An Ethiopian example. *Geology* 29, 527–530.
16
17
18 772 Ebinger, C.J., 1989. Geometric and kinematic development of border faults
19
773 and accommodation zones, Kivu-Rusizi rift, africa. *Tectonics* 8, 117–133.
20
21
22
23 774 Ellis, M., King, G., 1991. Structural control of flank volcanism in continental
24
775 rifts. *Science* 254, 839–842.
25
26
27
28 776 Faure, M., Lardeaux, J.M., Ledru, P., 2009. A review of the pre-Permian
29
777 geology of the Variscan French Massif Central. *Comptes rendus géoscience*
30
778 341, 202–213.
31
32
33
34 779 Forsyth, D., Uyeda, S., 1975. On the relative importance of the driving forces
35
780 of plate motion. *Geophysical Journal International* 43, 163–200.
36
37
38
39 781 Griffith, A.A., 1921. Vi. the phenomena of rupture and flow in solids. *Philo-*
40
782 *sophical Transactions of the Royal Society of London. Series A, containing*
41
783 *papers of a mathematical or physical character* 221, 163–198.
42
43
44
45 784 He, C., Dong, S., Chen, X., Santosh, M., Niu, S., 2014. Seismic evidence for
46
785 plume-induced rifting in the Songliao Basin of Northeast China. *Tectono-*
47
786 *physics* 627, 171–181.
48
49
50
51
52 787 Hinze, W.J., Allen, D.J., Fox, A.J., Sunwood, D., Woelk, T., Green, A.G.,
53
788 1992. Geophysical investigations and crustal structure of the North Amer-
54
789 ican Midcontinent Rift System. *Tectonophysics* 213, 17–32.
55
56
57
58

- 1
2
3
4
5
6
7
8
9
790 Hooper, A., Ófeigsson, B., Sigmundsson, F., Lund, B., Einarsson, P., Geirs-
10 son, H., Sturkell, E., 2011. Increased capture of magma in the crust pro-
11 moted by ice-cap retreat in iceland. *Nature Geoscience* 4, 783–786.
12
13
14
15
16
17
18
19
20
21
22
23
24
25
26
27
28
29
30
31
32
33
34
35
36
37
38
39
40
41
42
43
44
45
46
47
48
49
50
51
52
53
54
55
56
57
58
59
60
61
62
63
64
65
- 793 Hrubcová, P., Geissler, W.H., Bräuer, K., Vavryčuk, V., Tomek, Č., Kämpf,
794 H., 2017. Active magmatic underplating in western Eger Rift, central
795 Europe. *Tectonics* 36, 2846–2862.
- 796 Hyndman, R.D., Currie, C.A., Mazzotti, S.P., 2005. Subduction zone
797 backarcs, mobile belts, and orogenic heat. *GSA today* 15, 4–10.
- 798 Ito, G., Martel, S.J., 2002. Focusing of magma in the upper mantle through
799 dike interaction. *Journal of Geophysical Research: Solid Earth* 107, ECV–
800 6.
- 801 Ivanov, A., Demonterova, E., 2010. Extension in the Baikal rift and the
802 depth of basalt magma generation, in: *Doklady Earth Sciences*, Springer
803 Nature BV. p. 1564.
- 804 Jaeger, J.C., Cook, N.G., Zimmerman, R., 2009. *Fundamentals of rock me-*
805 *chanics*. John Wiley & Sons.
- 806 Janecke, S.U., Hammond, B.F., Snee, L.W., Geissman, J.W., 1997. Rapid
807 extension in an Eocene volcanic arc: Structure and paleogeography of
808 an intra-arc half graben in central Idaho. *Geological Society of America*
809 *Bulletin* 109, 253–267.
- 810 Keranen, K., Klemperer, S., Gloaguen, R., Group, E.W., 2004. Three-
811 dimensional seismic imaging of a protoridge axis in the Main Ethiopian
812 rift. *Geology* 32, 949–952.

- 1
2
3
4
5
6
7
8
9
10 813 Kohlstedt, D., Evans, B., Mackwell, S., 1995. Strength of the lithosphere:
11 814 Constraints imposed by laboratory experiments. *Journal of Geophysical*
12
13 815 *Research: Solid Earth* 100, 17587–17602.
- 14
15
16 816 Kühn, D., Dahm, T., 2008. Numerical modelling of dyke interaction and its
17
18 817 influence on oceanic crust formation. *Tectonophysics* 447, 53–65.
- 19
20
21 818 Kuzsnir, N.J., 1991. The distribution of stress with depth in the lithosphere:
22
23 819 thermo-rheological and geodynamic constraints. *Philosophical Transactions*
24
25 820 *of the Royal Society of London. Series A: Physical and Engineering*
26
27 821 *Sciences* 337, 95–110.
- 28
29 822 Liu, J., Han, J., Fyfe, W.S., 2001. Cenozoic episodic volcanism and continen-
30
31 823 tal rifting in northeast China and possible link to Japan Sea development
32
33 824 as revealed from K-Ar geochronology. *Tectonophysics* 339, 385–401.
- 34
35
36 825 Liu, L., Zoback, M.D., 1997. Lithospheric strength and intraplate seismicity
37
38 826 in the New Madrid seismic zone. *Tectonics* 16, 585–595.
- 39
40
41 827 Logatchev, N., Zorin, Y.A., 1992. Baikal rift zone: structure and geodynam-
42
43 828 ics. *Tectonophysics* 208, 273–286.
- 44
45 829 Lyngsie, S.B., Thybo, H., Lang, R., 2007. Rifting and lower crustal reflec-
46
47 830 tivity: A case study of the intracratonic Dniepr-Donets rift zone, Ukraine.
48
49 831 *Journal of Geophysical Research: Solid Earth* 112.
- 50
51
52 832 Maccaferri, F., Acocella, V., Rivalta, E., 2015. How the differential load
53
54 833 induced by normal fault scarps controls the distribution of monogenic vol-
55
56 834 canism. *Geophysical Research Letters* 42, 7507–7512.

- 1
2
3
4
5
6
7
8
9
835 Maccaferri, F., Bonafede, M., Rivalta, E., 2010. A numerical model of dyke
10 propagation in layered elastic media. *Geophysical Journal International*
11 180, 1107–1123.
12
13
14
15
16
838 Maccaferri, F., Bonafede, M., Rivalta, E., 2011. A quantitative study of the
17 mechanisms governing dike propagation, dike arrest and sill formation.
18 *Journal of Volcanology and Geothermal Research* 208, 39–50.
19
20
21
22
23
841 Maccaferri, F., Rivalta, E., Keir, D., Acocella, V., 2014. Off-rift volcanism in
24 rift zones determined by crustal unloading. *Nature Geoscience* 7, 297–300.
25
26
27
843 Maccaferri, F., Smittarello, D., Pinel, V., 2018. On the propagation path of
28 hydrofractures and magma-filled dykes: the competition between external
29 stress, internal pressure, and crack length., in: *EGU General Assembly*
30 *Conference Abstracts*, p. 8232.
31
32
33
34
35
847 Mackenzie, G., Thybo, H., Maguire, P., 2005. Crustal velocity structure
36 across the Main Ethiopian Rift: results from two-dimensional wide-angle
37 seismic modelling. *Geophysical Journal International* 162, 994–1006.
38
39
40
41
42
850 Mallard, C., Coltice, N., Seton, M., Müller, R.D., Tackley, P.J., 2016. Sub-
43 duction controls the distribution and fragmentation of Earth’s tectonic
44 plates. *Nature* 535, 140–143.
45
46
47
48
49
853 Mantiloni, L., Rivalta, E., Davis, T., 2023. Mechanical modeling of pre-
50 eruptive magma propagation scenarios at calderas. *Journal of Geophysical*
51 *Research: Solid Earth* 128, e2022JB025956.
52
53
54
55
56
57
58

- 1
2
3
4
5
6
7
8
9
10 856 Michon, L., Merle, O., 2001. The evolution of the Massif Central Rift; spatio-
11 857 temporal distribution of the volcanism. *Bulletin de la Société géologique*
12
13 858 *de France* 172, 201–211.
- 14
15
16 859 Modisi, M.P., Atekwana, E.A., Kampunzu, A., Ngwisanyi, T.H., 2000. Rift
17
18 860 kinematics during the incipient stages of continental extension: Evidence
19
20 861 from the nascent Okavango rift basin, northwest Botswana. *Geology* 28,
21
22 862 939–942.
- 23
24 863 Muller, O.H., Pollard, D.D., 1977. The stress state near Spanish Peaks,
25
26 864 Colorado determined from a dike pattern. *Pure and Applied Geophysics*
27
28 865 115, 69–86.
- 29
30
31 866 Nakamura, K., 1977. Volcanoes as possible indicators of tectonic stress ori-
32
33 867 entation—principle and proposal. *Journal of Volcanology and Geothermal*
34
35 868 *Research* 2, 1–16.
- 36
37
38 869 Neri, M., Rivalta, E., Maccaferri, F., Acocella, V., Cirrincione, R., 2018.
39
40 870 Etnean and Hyblean volcanism shifted away from the Malta Escarpment
41
42 871 by crustal stresses. *Earth and Planetary Science Letters* 486, 15–22.
- 43
44 872 Oliva, S.J., Ebinger, C.J., Rivalta, E., Williams, C.A., Wauthier, C., Currie,
45
46 873 C.A., 2022. State of stress and stress rotations: Quantifying the role of
47
48 874 surface topography and subsurface density contrasts in magmatic rift zones
49
50 875 (Eastern Rift, Africa). *Earth and Planetary Science Letters* 584, 117478.
- 51
52
53 876 Pasteels, P., Villeneuve, M., De Paepe, P., Klerkx, J., 1989. Timing of the
54
55 877 volcanism of the southern Kivu province: implications for the evolution of
56
57
58
59
60
61
62
63
64
65

- 1
2
3
4
5
6
7
8
9
878 the western branch of the East African Rift system. *Earth and Planetary*
10
879 *Science Letters* 94, 353–363.
11
12
13
14 880 Pollard, D.D., 1987. Elementary fracture mechanics applied to the structural
15
881 interpretation of dykes, in: *Mafic dyke swarms*. Geological Association of
16
882 Canada. volume 34, pp. 5–24.
17
18
19
20
883 Rivalta, E., Corbi, F., Passarelli, L., Acocella, V., Davis, T., Di Vito, M.A.,
21
884 2019. Stress inversions to forecast magma pathways and eruptive vent
22
885 location. *Science advances* 5, eaau9784.
23
24
25
26
886 Rivalta, E., Taisne, B., Bungler, A., Katz, R., 2015. A review of mechan-
27
887 ical models of dike propagation: Schools of thought, results and future
28
888 directions. *Tectonophysics* 638, 1–42.
29
30
31
32
33
889 Roman, A., Jaupart, C., 2014. The impact of a volcanic edifice on intrusive
34
890 and eruptive activity. *Earth and Planetary Science Letters* 408, 1–8.
35
36
37
38
891 Rubin, A.M., 1993. Dikes vs. diapirs in viscoelastic rock. *Earth and Planetary*
39
892 *Science Letters* 117, 653–670.
40
41
42
43 893 Rubin, A.M., 1995. Propagation of magma-filled cracks. *Annual Review of*
44
894 *Earth and Planetary Sciences* 23, 287–336.
45
46
47
48 895 Ruppel, C., 1995. Extensional processes in continental lithosphere. *Journal*
49
896 *of Geophysical Research: Solid Earth* 100, 24187–24215.
50
51
52
53 897 Secor Jr, D.T., Pollard, D.D., 1975. On the stability of open hydraulic
54
898 fractures in the Earth’s crust. *Geophysical Research Letters* 2, 510–513.
55
56
57
58

- 1
2
3
4
5
6
7
8
9 899 Sigmundsson, F., Hooper, A., Hreinsdóttir, S., Vogfjörð, K.S., Ófeigsson,
10 B.G., Heimisson, E.R., Dumont, S., Parks, M., Spaans, K., Gudmundsson,
11 G.B., et al., 2015. Segmented lateral dyke growth in a rifting event at
12
13 901 Bárðarbunga volcanic system, Iceland. *Nature* 517, 191–195.
14
15 902
16
17 903 Thybo, H., Artemieva, I., 2013. Moho and magmatic underplating in conti-
18
19 904 nental lithosphere. *Tectonophysics* 609, 605–619.
20
21
22 905 Thybo, H., Nielsen, C., 2009. Magma-compensated crustal thinning in con-
23
24 906 tinental rift zones. *Nature* 457, 873–876.
25
26
27 907 Turcotte, D.L., 1979. Flexure, in: *Advances in geophysics*. Elsevier. vol-
28
29 908 ume 21, pp. 51–86.
30
31
32 909 Watanabe, T., Masuyama, T., Nagaoka, K., Tahara, T., 2002. Analog ex-
33
34 910 periments on magma-filled cracks: Competition between external stresses
35
36 911 and internal pressure. *Earth, planets and space* 54, e1247–e1261.
37
38
39 912 Weertman, J., 1971. Theory of water-filled crevasses in glaciers applied to
40
41 913 vertical magma transport beneath oceanic ridges. *Journal of Geophysical*
42
43 914 *Research* 76, 1171–1183.
44
45 915 Wenzel, F., Brun, J.P., Group, E.D.W., et al., 1991. A deep reflection seismic
46
47 916 line across the northern rhine graben. *Earth and Planetary Science Letters*
48
49 917 104, 140–150.
50
51
52 918 White, R., 1992. Magmatism during and after continental break-up. *Geo-*
53
54 919 *logical Society, London, Special Publications* 68, 1–16.
55
56
57
58
59
60
61
62
63
64
65

1
2
3
4
5
6
7
8
9
10
11
12
13
14
15
16
17
18
19
20
21
22
23
24
25
26
27
28
29
30
31
32
33
34
35
36
37
38
39
40
41
42
43
44
45
46
47
48
49
50
51
52
53
54
55
56
57
58
59
60
61
62
63
64
65

920 Zeyen, H., Novak, O., Landes, M., Prodehl, C., Driad, L., Hirn, A., 1997.
921 Refraction-seismic investigations of the northern Massif Central (France).
922 Tectonophysics 275, 99–117.

923 Ziv, A., Rubin, A.M., Agnon, A., 2000. Stability of dike intrusion along
924 preexisting fractures. Journal of Geophysical Research: Solid Earth 105,
925 5947–5961.

926 Zoback, M.D., Townend, J., 2001. Implications of hydrostatic pore pressures
927 and high crustal strength for the deformation of intraplate lithosphere.
928 Tectonophysics 336, 19–30.